Non-Hydrostatic RegCM4 (RegCM4-NH): Model description and case studies over multiple domains.

Coppola E. (1), Stocchi P. (2), Pichelli E. (1), Torres A. (1), Glazer R. (1), Giuliani G. (1), F. Di Sante (1), R. Nogherotto (1), Giorgi F. (1)

Correspondence to: Erika Coppola (coppolae@ictp.it)

1. International Centre for Theoretical Physics (ICTP),Trieste, Italy
2. Institute of Atmospheric Sciences and Climate, National Research Council of Italy, CNR-ISAC, Bologna, Italy

Abstract. We describe the development of a non-hydrostatic version of the regional climate model RegCM4, called RegCM4-NH, for use at convection-permitting resolutions. The non-hydrostatic dynamical core of the Mesoscale Model MM5 is introduced in the RegCM4, with some modifications to increase stability and applicability of the model to long-term climate simulations. Newly available explicit microphysics schemes are also described, and three case studies of intense convection events are carried out in order to illustrate the performance of the model. They are all run at convection-permitting grid spacing of 3 km over domains in northern California, Texas and the Lake Victoria region, without the use of parameterized cumulus convection. A substantial improvement is found in several aspects of the simulations compared to corresponding coarser resolution (12 km) runs completed with the hydrostatic version of the model employing parameterized convection. RegCM4-NH is currently being used in different projects for regional climate simulations at convection-permitting resolutions, and is intended to be a resource for users of the RegCM modeling system.

Keywords

Regional climate models; RegCM4; km-scale resolution; climate change

Formatted: Numbering: Continuous

Introduction

Since the pioneering work of Dickinson et al. (1989) and Giorgi and Bates (1989), documenting the first regional climate modeling system (RegCM, version 1) in literature, the dynamical downscaling technique based on limited area Regional Climate Models (RCMs) has been widely used worldwide, and a number of RCM systems have been developed (Giorgi 2019). RegCM1 (Dickinson et al., 1989, Giorgi and Bates, 1989) was originally developed at the National Center for Atmospheric Research (NCAR) based on the Mesoscale Model version 4 (MM4) (Anthes et al, 1987) . Then, further model versions followed: RegCM2 (Giorgi et al. 1993a,b), RegCM2.5, (Giorgi and Mearns 1999), RegCM3 (Pal et al. 2007), and lastly RegCM4 (Giorgi et al 2012). Except for the transition from RegCM1 to RegCM2, in which the model dynamical core was updated from that of the MM4 to that of the MM5 (Grell et al. 1995), these model evolutions were mostly based on additions of new and more advanced physics packages. RegCM4 is today used by a large community for numerous projects and applications, from process studies to paleo and future climate projections, including participation in the Coordinated Regional Downscaling EXperiment (CORDEX, Giorgi et al. 2009; Gutowski et al. 2016). The model can also be coupled with ocean, land and chemistry/aerosol modules in a fully interactive way (Sitz et al. 2017).

The dynamical core of the standard version of RegCM4 is hydrostatic, with sigma-p vertical coordinates. As a result, the model can be effectively run for grid spacings of ~10 km or larger, for which the hydrostatic assumption is valid. However, the RCM community is rapidly moving to higher resolutions of a few km, i.e. “convection-permitting” (Prein et al. 2015; Coppola et al. 2020) and therefore the dynamical core of RegCM4 has been upgraded to include a non-hydrostatic dynamics representation usable for very high resolution applications. This upgrade, which we name RegCM4-NH, is essentially based on the implementation of the MM5 non-hydrostatic dynamical core within the RegCM4 framework, which has an entirely different set of sub-grid model physics compared to MM5.

RegCM4-NH is already being used in some international projects focusing on climate simulations at convection-permitting km-scales, namely the European Climate Prediction

System (EUCP, Hewitt and Lowe 2018) and the CORDEX Flagship Pilot Study dedicated to convection (CORDEX-FPSCONV, Coppola et al. 2020), and it is starting to be used more broadly by the RegCM modeling community.

For example, the recent papers by Ban et al. (2021) and Pichelli et al. (2021) document results of the first multi-model experiment of 10-year simulations at the convection-permitting scales over the so-called greater Alpine region. Two different simulations with RegCM4-NH for present day conditions have contributed to the evaluation analysis of Ban et al. (2021). They were carried out at the International Centre for Theoretical Physics (ICTP) and the Croatian Meteorological and Hydrological Service (DHMZ) using two different physics configurations. The results show that RegCM4-NH largely improves the precipitation simulation as compared to available fine scale observations when going from coarse to high resolution, in particular for higher order statistics, such as precipitation extremes and hourly intensity. Pichelli et al. (2021) then analyse multi-model ensemble simulations driven by selected CMIP5 GCM projections for the decades 1996–2005 and 2090–2099 under the RCP8.5 scenario. ICTP contributed to the experiment with simulations using RegCM4-NH driven by the MOCH-HadGEM GCM (r1i1p1) in a two level nest configuration (respectively at 12 and 3 km grid). The paper shows new insights into future changes, for example an enhancement of summer and autumn hourly rainfall intensification compared to coarser resolution model experiments, as well as an increase of frequency and intensity of high-impact weather events.

In this paper we describe the structure of RegCM4-NH and provide some illustrative examples of its performance, so that model users can have a basic reference providing them with background information on the model. In the next section we first describe the new model dynamical core, while the illustrative applications are presented in section 4. Section 5 finally provides some discussion of future developments planned for the RegCM system.

Model description

In the development of RegCM4-NH, the RegCM4 as described by Giorgi et al. (2012) was modified to include, the non-hydrostatic dynamical core (*idynamic* = 2 namelist option as described in RegCM-4.7.1/Doc/README.namelist of the source code) of the mesoscale model MM5 (Grell et al. 1995). This dynamical core was selected because RegCM4 already has the same grid and variable structure as MM5 in its hydrostatic core, which substantially facilitated its implementation (Elguindi et al. 2017).

Deleted:

The model equations with complete description of the Coriolis force and a top radiative boundary condition, along with the finite differencing scheme, are given in Grell et al. (1995). Pressure, p, temperature, T, and density, ϱ, are first decomposed into a prescribed reference vertical profile plus a time varying perturbation. The prognostic equations are then calculated using the pressure perturbation values. Compared to the original MM5 dynamical core, the following modifications were implemented in order to achieve increased stability for long term climate simulations (Elguindi et al. 2017 document any modifications which follow the choice of the non-hydrostatic dynamical core through the namelist parameter *idynamic* = 2; further available user-dependant options, and the corresponding section in the namelist, are explicitly indicated):

i) The reference state temperature profile is computed using a latitude dependent climatological temperature distribution and thus is a function of the specific domain coordinates (*base_state_pressure*, *logp_lrate* parameters in *&referenceatm*) (Elguindi et al. 2017). These two parameters were hard-coded in the original MM5 while for the RegCM are user configurable;

ii) The lateral time dependent boundary conditions (*iboudy* in *&physicsparam*) for each prognostic variable use the same exponential relaxation technique (*iboudy* = 5) described in Giorgi et al. (1993). The linear MM5 relaxation scheme is also kept as an option (*iboudy* = 1);

iii) The advection term in the model equations, which in the MM5 code is implemented using a centered finite difference approach, was changed to include a greater upstream weight factor as a function of the local Courant number (Elguindi et al. 2017). The maximum value of the weight factor is user configurable (*uoffc* in *&dynparam*). As detailed in the MM5 model description (Grell et al, 1995), the horizontal advection term for a scalar variable X contributes to the total tendency as:

$$\Delta_{adv}\left(p^{*}X\right)_{G} = -m^{2}|_{G}\left[\frac{\left(p^{*}X|_{b}\frac{u}{m}|_{b} - p^{*}X|_{a}\frac{u}{m}|_{a}\right)}{dx} + \frac{\left(p^{*}X|_{d}\frac{v}{m}|_{d} - p^{*}X|_{c}\frac{v}{m}|_{c}\right)}{dy}\right]$$

where the m is the projection mapping factor and, with respect to Figure 1, assuming that the computation is to be performed for the gold cross point G, the averages are performed in the points a, b, c, d. For the u/m and v/m terms, the average value is computed using respectively the values in points AC, BD, CD, AB.

In RegCM4 for the term $p^{*}X$, the model computes a weighted average value of the field using the value in gold+cyan and gold+green cross points with weights increasing the relative contribution of the upstream point up as a function of the local courant number:

$$p^{*}X|_{a} = 0.5((1-f_{1})p^{*}X|_{G} + (1+f_{1})p^{*}X|_{c_{1}})$$
$$p^{*}X|_{b} = 0.5((1-f_{1})p^{*}X|_{c_{2}} + (1+f_{1})p^{*}X|_{G})$$
$$p^{*}X|_{c} = 0.5((1-f_{2})p^{*}X|_{G} + (1+f_{2})p^{*}X|_{g_{1}})$$
$$p^{*}X|_{d} = 0.5((1-f_{2})p^{*}X|_{g_{2}} + (1+f_{2})p^{*}X|_{G})$$

where f_{1}, f_{2} are defined as the local Courant number for the 1D advection equations multiplied for a control factor:

$$f_{1} = \mu_{fc}dt\frac{(u|_{a} + u|_{b})}{2dx}$$
$$f_{2} = \mu_{fc}dt\frac{(v|_{c} + v|_{d})}{2dy}$$
;

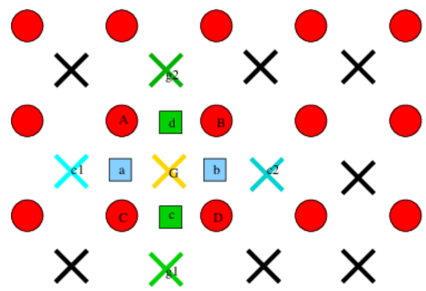

Figure 1 Schematic representation showing the horizontal advection scheme staggering. Circles are U,V points. X are scalar variable points.

iv) The moisture term uses the same advection scheme as the other variables (Elguindi et al. 2017) and not a complete upstream scheme as in the MM5 code (Grell et al. 1995);

v) A local flux limiter reduces the advection terms in order to remove unrealistic strong gradients and its limits are user configurable (in the *&dynparam* section the maximum gradient fraction for advection: temperature, *t_extrema*, specific humidity, *q_rel_extrema*, liquid cloud content, *c_rel_extrema* and for tracers, *t_rel_extrema*). This was hardcoded in the MM5 code and the limits were not user configurable;

vi) The diffusion stencil of the Laplace equation uses a nine point approach as in LeVeque (2006) and a topography dependent environmental diffusion coefficient is added to reduce spurious diffusion along pressure coordinate slopes (Elguindi et al. 2017) as in the hydrostatic version of the code (Giorgi et al. 1993b). The change in stencil does not affect the overall fourth order precision of the model, but reduces the computational stencil size, thus reducing the communication overhead;

vii) The top boundary radiative condition (*ifupr* = 1 in *&nonhydroparam*) adopted in the semi-implicit vertical differencing scheme to reduce the reflection of energy waves uses coefficients on a 13x13 matrix which are re-computed every simulation day and not kept constant throughout the whole simulation as in the MM5 code. This allows the model to

Deleted:

be run for longer simulation times while not being strongly tied to the intial atmospheric conditions;

viii) The dynamical control parameter β in the semi-implicit vertical differencing scheme (*nhbet* in *&nonhydroparam*) used for acoustic wave damping (Elguindi et al. 2017) is user configurable (Klemp and Dudhia, 2008), while it is hard-coded in the MM5;

ix) A Rayleigh damping (*ifrayd* = 1 in *&nonhydroparam*) of the status variables towards the input GCM boundary conditions can be activated in the top layers (*rayndamp* configuring the number of top levels to apply) with a configurable relaxation time (*rayalpha0*, Klemp and Lilly, 1978, Durran and Klemp, 1983. This is consistent to what is implemented in the WRF model);

x) The water species time filtering uses the Williams (2009) modified filter with α = 0.53 instead of the RA filter used by all the other variables. The ν factor in the RA filter is user configurable (*gnu1* and *gnu2* in *&dynparam*). This reduces the damping introduced by the Robert-Asselin filter and the computational diffusion introduced by the horizontal advection scheme.

With these modifications, the model basic equations, under leap-frog integration scheme, are (Elguindi et al. 2017) :

$$\frac{\partial p^* u}{\partial t} = -m^2 \left[\frac{\partial p^* u u/m}{\partial x} + \frac{\partial p^* v u/m}{\partial y} \right] - \frac{\partial p^* u \dot{\sigma}}{\partial \sigma} + uDIV - \frac{mp^*}{\rho} \left[\frac{\partial p'}{\partial x} - \frac{\sigma}{p^*} \frac{\partial p^*}{\partial x} \frac{\partial p'}{\partial \sigma} \right] + p^* f v - p^* e w \cos\theta + D_u \quad (1)$$

$$\frac{\partial p^* v}{\partial t} = -m^2 \left[\frac{\partial p^* u v/m}{\partial x} + \frac{\partial p^* v v/m}{\partial y} \right] - \frac{\partial p^* v \dot{\sigma}}{\partial \sigma} + vDIV - \frac{mp^*}{\rho} \left[\frac{\partial p'}{\partial y} - \frac{\sigma}{p^*} \frac{\partial p^*}{\partial y} \frac{\partial p'}{\partial \sigma} \right] - p^* f u + p^* e w \sin\theta + D_v \quad (2)$$

$$\frac{\partial p^* w}{\partial t} = -m^2\left[\frac{\partial p^* u w/m}{\partial x} + \frac{\partial p^* v w/m}{\partial y}\right] - \frac{\partial p^* w\dot{\sigma}}{\partial \sigma} + wDIV +$$

$$p^* g \frac{\rho_0}{\rho}\left[\frac{1}{p^*}\frac{\partial p'}{\partial \sigma} + \frac{T_v'}{T} - \frac{T_0 p'}{T p_0}\right] - p^* g\left[(q_c + q_r)\right] + p^* e\left(u\cos\theta - v\sin\theta\right) + D_w \quad (3)$$

$$\frac{\partial p^* p'}{\partial t} = -m^2\left[\frac{\partial p^* u p'/m}{\partial x} + \frac{\partial p^* v p'/m}{\partial y}\right] - \frac{\partial p^* p'\dot{\sigma}}{\partial \sigma} + p' DIV -$$

$$m^2 p^* \gamma p\left[\frac{\partial u/m}{\partial x} - \frac{\sigma}{m p^*}\frac{\partial p^*}{\partial x}\frac{\partial u}{\partial \sigma} + \frac{\partial v/m}{\partial y} - \frac{\sigma}{m p^*}\frac{\partial p^*}{\partial y}\frac{\partial v}{\partial \sigma}\right] + \rho_0 g \gamma p \frac{\partial w}{\partial \sigma} + p^* \rho_0 g \quad (4)$$

$$\frac{\partial p^* T}{\partial t} = -m^2\left[\frac{\partial p^* u T/m}{\partial x} + \frac{\partial p^* v T/m}{\partial y}\right] - \frac{\partial p^* T\dot{\sigma}}{\partial \sigma} + TDIV +$$

$$\frac{1}{\rho c_p}\left[p^* \frac{Dp'}{Dt} - \rho_0 g p^* w - D_{p'}\right] + p^* \frac{\dot{Q}}{c_p} + D_T \quad (5)$$

Where:

$$DIV = m^2\left[\frac{\partial p^* u/m}{\partial x} + \frac{\partial p^* v/m}{\partial y}\right] + \frac{\partial p^* \dot{\sigma}}{\partial \sigma}$$

$$\dot{\sigma} = -\frac{\rho_0 g}{p^*} w - \frac{m\sigma}{p^*}\frac{\partial p^*}{\partial x} u - \frac{m\sigma}{p^*}\frac{\partial p^*}{\partial y} v$$

$$\tan\theta = -\cos\phi \frac{\partial \lambda/\partial y}{\partial \phi/\partial x}$$

$$p(x,y,z,t) = p_0(z) + p'(x,y,z,t)$$

$$T(x,y,z,t) = T_0(z) + T'(x,y,z,t)$$

$$\rho(x,y,z,t) = \rho_0(z) + \rho'(x,y,z,t)$$

with the vertical sigma coordinate defined as:

$$\sigma = \frac{(p_0 - p_t)}{(p_s - p_t)}$$

p_s is the surface pressure and p_0 is the reference pressure profile. The total pressure at each grid point is thus given as:

$$p(x, y, z, t) = p^* \sigma(k) + p_t + p'(x, y, z, t)$$

With p_t being the top model pressure assuming a fixed rigid lid.

The model physics schemes for boundary layer, radiative transfer, land and ocean surface processes, cloud and precipitation processes are extensively described in Giorgi et al. (2012) and summarized in Table 1. For each physics component a number of parameterization options are available (Table 1), and can be selected using a switch selected by the user. As mentioned, the use of non-hydrostatic dynamics is especially important when going to convection-permitting resolutions of a few km (Prein et al. 2015). At these resolutions the scale separation assumption underlying the use of cumulus convection schemes is not valid any more, and explicit cloud microphysics representations are necessary. The RegCM4 currently includes two newly implemented microphysics schemes, the Nogherotto-Tompkins (Nogherotto et al. 2016) and the WSM5 scheme from the Weather Research Forecast (WRF, Skamarok et al. 2008) model, which are briefly described in the next sections for information to model users.

Model physics (*Namelist flag*)	**Options**	***n. option***	**Reference**
Dynamical core (*idynamic*)	Hydrostatic	1	Giorgi et al. 1993a,b Giorgi et al. 2012
	Non-Hydrostatic (*)	2	present paper
Radiation (*irrtm*)	CCSM	0	Kiehl et al. 1996
	RRTM (*)	1	Mlawer et al. 1997
Microphysics	Subex	1	Pal et al 2000

(*ipptls*)	Nogherotto Thompkins	2	Nogherotto et al. 2016
	WSM5 (*)	3	Hong et al 2004
Cumulus (*icup*)	Kuo	1	Anthes et al. 1987
	Grell	2	Grell 1993
	Emanuel	4	Emanuel 1991
	Tiedtke	5	Tiedtke 1989, 1993
	Kain-Fritsch	6	Kain and Fritsch, 1990; Kain 2004
	MM5 Shallow cumulus (only mixing) (*)	-1	Grell et al. 1994
Planetary Boundary Layer (*ibltyp*)	Modified-Holtslag	1	Holtslag et al., 1990
	UW	2	Bretherton et al. 2004
Land Surface (*code compiling option*)	BATS	/	Dickinson et al. 1993; Giorgi et al. 2003
	CLM4.5	/	Oleson et al. 2013
Ocean Fluxes (*iocnflx*)	BATS	1	Dickinson et al. 1993
	Zeng	2	Zeng et al. 1998
	COARE	3	Fairall et al. 1996a,b

Interactive lake (*lakemod*)	1D diffusion/convection	1	Hostetler et al. 1993
Tropical band (*i_band*)	RegT-Band	1	Coppola et al. 2012
Coupled ocean (*iocncpl*)	RegCM-ES	1	Sitz et al. 2017

Table 1 Core and sub-grid physics scheme available in RegCM-NH. New schemes available with this release are starred (*).

Explicit microphysics schemes

Nogherotto-Tompkins Scheme

A new parameterization for explicit cloud microphysics and precipitation built upon the European Centre for Medium Weather Forecast's Integrated Forecast System (IFS) module (Tiedtke [1993], Tompkins [2007]), was introduced in RegCM4 (*ipptls* = 2 in *&microparam*) by Nogherotto et al. [2016]. In the present configuration, the scheme implicitly solves 5 prognostic equations for water vapor, qv, cloud liquid water, ql, rain, qr, cloud ice, qi, and snow, qs, but it is also easily extendable to a larger number of variables. Water vapor, cloud liquid water, rain, cloud ice and snow are all expressed in terms of the grid-mean mixing ratio.

Deleted:

Cloud liquid and ice water content are independent, allowing the existence of supercooled liquid water and mixed-phase clouds. Rain and snow precipitate with a fixed terminal fall speed and can then be advected by the three dimensional winds. A check for the conservation of enthalpy and of total moisture is ensured at the end of each timestep. The governing equation for each variable is:

$$\frac{\partial q_x}{\partial t} = S_x + \frac{1}{\rho}\frac{\partial}{\partial z}(\rho V_x q_x)$$

The local variation of the mixing ratio qx of the variable x is given by the sum of Sx, containing the net sources and sinks of qx through microphysical processes (i.e. condensation, evaporation, auto-conversion, melting, etc.), and the sedimentation term, which is a function of the fall speed Vx . An upstream approach is employed to solve the equations. The sources and sinks contributors are divided in two groups according to the duration of the process they describe: processes that are considered to be fast relative to the model time step are treated implicitly while slow processes are treated explicitly. The processes taken into account (shown in Figure 2) are the microphysical pathways across the 5 water variables: condensation, autoconversion, evaporation, cloud water collection (accretion), and autoconversion for warm clouds, and freezing, melting, deposition, sublimation for cold clouds.

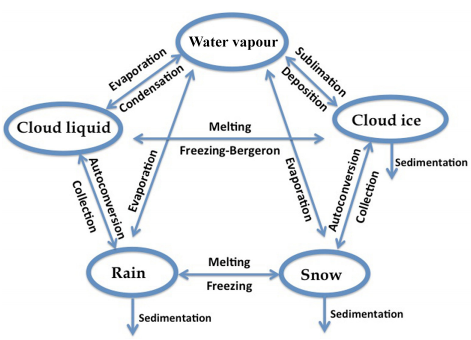

Figure 2: Depiction of the new scheme, showing the five prognostic variables and how they are related to each other through microphysical processes

For each microphysical pathway, phase changes are associated with the release or absorption of latent heat, which then impacts the temperature budget. The impact is calculated using the conservation of liquid water temperature TL defined as:

$$T_L = T - \frac{L_v}{C_p}(q_l + q_r) - \frac{L_s}{C_p}(q_i + q_s).$$

Given that dTL =0, the rate of change of the temperature is given by the following equation:

$$\frac{\partial T}{\partial t} = \sum_{x=1}^{m} \frac{L(x)}{C_p}\left(\frac{dq_x}{dt} - D_{q_x} - \frac{1}{\rho}\frac{\partial}{\partial z}(\rho V_x q_x)\right)$$

where *L*(*x*) is the latent heat of fusion or evaporation, depending on the process considered, *Dqx* is the convective detrainment and the third term in brackets is the sedimentation term.

At the end of each time step a check is carried out of the conservation of total water and moist static energy: $h = C_P T + gz + Lq_x.$

The scheme is tunable through parameters in the *&microparam* section of the namelist (RegCM-4.7.1/Doc/README.namelist; Elguindi et al. 2017).

WSM5 Scheme

RegCM4-NH also employs the Single-Moment 5-class microphysics scheme of the WRF model (Skamarock et al., 2008). This scheme (ipptls = 3 in &microparam) follows Hong et al. (2004) and, similarly to Nogherotto et al. (2016), includes vapor, rain, snow, cloud ice, and cloud water hydrometeors. The scheme separately treats ice and water saturation processes, assuming water hydrometeors for temperatures above freezing, and cloud ice and snow below the freezing level (Dudhia, 1989, Hong et al., 1998). It accounts for supercooled water and a gradual melting of snow below the melting layer

Deleted:

(Hong et al., 2004, and Hong and Lim, 2006). Therefore, the WSM5 and Nogherotto-Tompkins schemes have similar structures (Figure 1), but also important differences.

Differently from the Nogherotto-Tompkins scheme, the WSM5 (as well as the other WSM schemes in WRF) prescribes an inverse exponential continuous distribution of particle size (ex. Marshall and Palmer (1948) for rain, Gunn and Marshall (1958) for snow). It also includes the size distribution of ice particles and, as a major novelty, the definition of the number of ice crystals based on ice mass content rather than temperature. Both the Nogherotto-Tompkins and WSM5 schemes include autoconversion, i.e. sub-time step processes of conversion of cloud water to rain and cloud ice to snow. For rain, Hong et al. (2004) use a Kessler (1969) type algorithm in WSM5, but with a stronger physical basis following Tripoli and Cotton (1980). The Nogherotto-Tompkins scheme also includes the original Kessler (1969) formula as an option, but it makes available other three exponential approaches following Sundqvist et al. (1989), Beheng (1994), and Khairoutdinov and Kogan (2000). For ice autoconversion the Nogherotto-Tompkins scheme uses an exponential approach (Sundqvist, 1989) with a specific coefficient for ice particles (following Lin et al., 1983) depending on temperature, while the WSM5 uses a critical value of ice mixing ratio (depending on air density) and a maximum allowed ice crystal mass (following Rutledge and Hobbs, 1983) that suppresses the process at low temperatures because of the effect of air density. Finally, the WSM5 has no dependency on cloud cover for condensation processes while the Nogherotto-Tompkins scheme uses cloud cover to regulate the condensation rate in the formation of stratiform clouds.

Illustrative case studies

Three case studies (Table 2) of Heavy Precipitation Events (HPE) have been identified in order to test and illustrate the behavior of the non-hydrostatic core of the RegCM4-NH, with focus on the explicit simulation of convection over different regions of the world. In two of the test cases, California and Lake Victoria, data from the ERA-Interim reanalysis (Dee et al. 2011) are used to provide initial and lateral meteorological boundary conditions (every 6 hours) for an intermediate resolution run (grid spacing of 12 km, with use of convection parameterizations), which then provides driving boundary conditions for the convection-permitting experiments (Figure 3). In the Texas case study, however, we nested the model directly in the ERA-Interim reanalysis given that such configuration was able to accurately reproduce the HPE intensity. In this case the model uses a large LBC relaxation zone which allows the description of realistic fine-scale features driving this weather event (although not fully consistent with the Matte et al. (2017) criteria). All simulations start 24-48 hours before the HPE (Table 2). The analysis focuses on the total accumulated precipitation over the entire model domain at 3 km resolution (Figure 2) for the periods defined in Table 2. In the cases of California and Texas the evaluation also includes the time series of 6 hourly accumulated precipitation averaged on the region of maximum precipitation (black rectangles in Figures 5a and 7a) because high temporal resolution observations (NCEP/CPC) are also available (Table 3). The discussion of the case studies is presented in the next sections; the configuration files (namelists) with full settings for the three test cases are available at https://zenodo.org/record/5106399.

Deleted:
Deleted: (Figure 3)
Deleted:
Deleted: with boundary conditions provided every 6 hours,…
Deleted:
Deleted: accurately
Deleted: even if
Deleted: .
Deleted: .
Deleted: 1
Deleted: s.
Deleted:
Deleted: 4,
Deleted: against available
Deleted: (Table 2)

A key issue concerning the use of CP-RCMs is the availability of very high resolution, high quality observed datasets for the assessment and evaluation of the models, which is lacking for most of the world regions. Precipitation measurements come from essentially three distinct sources: in-situ rain-gauges, ground radar and satellite. In the present study we use 7 observational datasets depending on the case study and the area covered, as described in Table 3. We have used: Precipitation Estimation from Remotely Sensed Information using Artificial Neural Networks - Climate Data Record (PERSIAN-CDR), Climate Hazards Group InfraRed Precipitation with Station data (CHIRPS), the Climate Prediction Center morphing method (CMORPH), Tropical Rainfall Measuring Mission (TRMM), NCEP/CPC-Four Kilometer Precipitation Set Gauge and Radar (NCEP/CPC), CPC-Unified gauge-based daily precipitation estimates (CPC) and Parameter-elevation Regressions on Independent Slopes Model (PRISM) (Table 3). NCEP/CPC is a precipitation analysis which merges a rain gauge dataset with radar estimates. CMORPH and PERSIAN-CDR are based on satellite measurements, CHIRPS incorporates satellite imagery with in-situ station data. CPC is a gauge-based analysis of

Deleted: not there
Deleted: 2
Deleted: daily
Deleted: guage
Deleted:

daily precipitation. The PRISM dataset gathers climate observations from a wide range of monitoring networks, applying sophisticated quality control measures and developing spatial climate datasets which incorporate a variety of modeling techniques at multiple spatial and temporal resolutions.

Deleted: and t

Deleted: ies

Deleted: ,

Deleted: s

Deleted: incorporating

Case	ACRONYM	Region of The event	Domains size lon x lat x vertical levels	Simulation Time Window (UTC)
1	CAL	California	480 x 440 x 41	15 Feb 2004 00:00 19 Feb 2004 00:00
2	TEX	Texas	480 x 440 x 41	9 June 2010 00:00 12 June 2010 00:00
3	LKV	Lake Victoria	550 x 530 x 41	25 Nov 1999 00:00 1 Dec 1999 00:00

Table 2: List of acronyms and description of the test cases with corresponding 3km domain sizes and simulation period.

Dataset name	Region	Spatial Resolution	Temporal Resolution	Data Source	Reference
TRMM	World	0.5°	Daily	Satellite	Huffman et al. (2007)
CHIRPS	World	0.05°	Daily	Station data+Satellite	Funk et al. (2015)
CMORPH	World	0.25°	Daily	Satellite	Joyce et al.

					(2004)
NCEP/CPC	USA	0.04°	Hourly	*Gauge and Radar*	https://doi.org/10.5065/D69Z93M3. Accessed: 27/06/2018
CPC	World	0.5°	Daily	Station data	Chen and Xie (2008)
PRISM	USA	0.04°	Daily	Station data	PRISM Climate Group. 2016.
PERSIAN-CDR	World	0.25°	Daily	Satellite	Ashouri et al. (2015)

Table 3: List of observed precipitation datasets used for comparison.

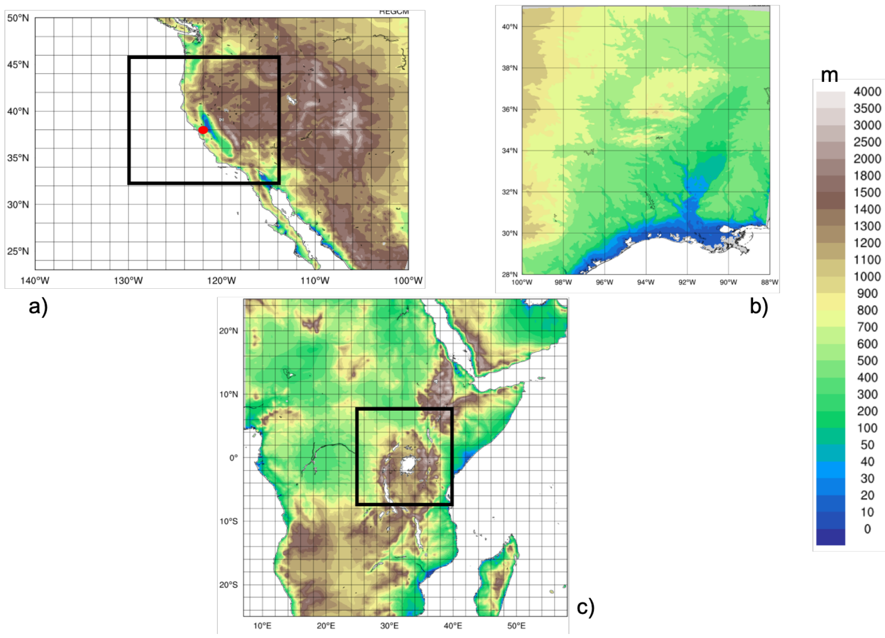

Figure 3: Domains tested , a) California (CAL) , b) Texas (TEX), c) Lake Victoria (LKV) . For CAL (a) and LKV (b) the black square shows the 3 km simulation domains nested in the 12 km domain in figure. For TEX case (b) the 3 km domain simulation (b) is fed directly with the ERA-Interim reanalysis fields.

Deleted: Simulation d

Deleted: c

California

The first case, referred to as CAL in Table 2, is a HPE which occurred on February 16-18 2004, producing flooding conditions for the Russian River, a southward-flowing river in the Sonoma and Mendocino counties of northern California (red-dot in Figure 3a). The event is documented in detail by Ralph et al. (2006), who focused their attention on the impact of narrow filament-shaped structures of strong horizontal water vapor transport over the eastern Pacific Ocean and the western U.S. coast, called Atmospheric Rivers

Deleted: (California)

Deleted: 1

Deleted: 16–18

Deleted:) (

(ARs). ARs are typically associated with a low-level jet stream ahead of the cold front of extratropical cyclones (Zhu and Newell 1998; Dacre et al. 2015; Ralph et al. 2018), and can induce heavy precipitation where they make landfall and are forced to rise over mountain chains (Gimeno et al. 2014). The CAL event consists of a slow propagating surface front arching southeastward towards Oregon and then southwestward offshore of California (Figure 4a,c). Rain began over the coastal mountains of the Russian River watershed at 0700 UTC of February 16, as a warm front descended southward, and also coincided with the development of orographically favoured low-level upslope flow (Ralph et al., 2006).

Deleted: .3

Deleted: , 16

Deleted: (

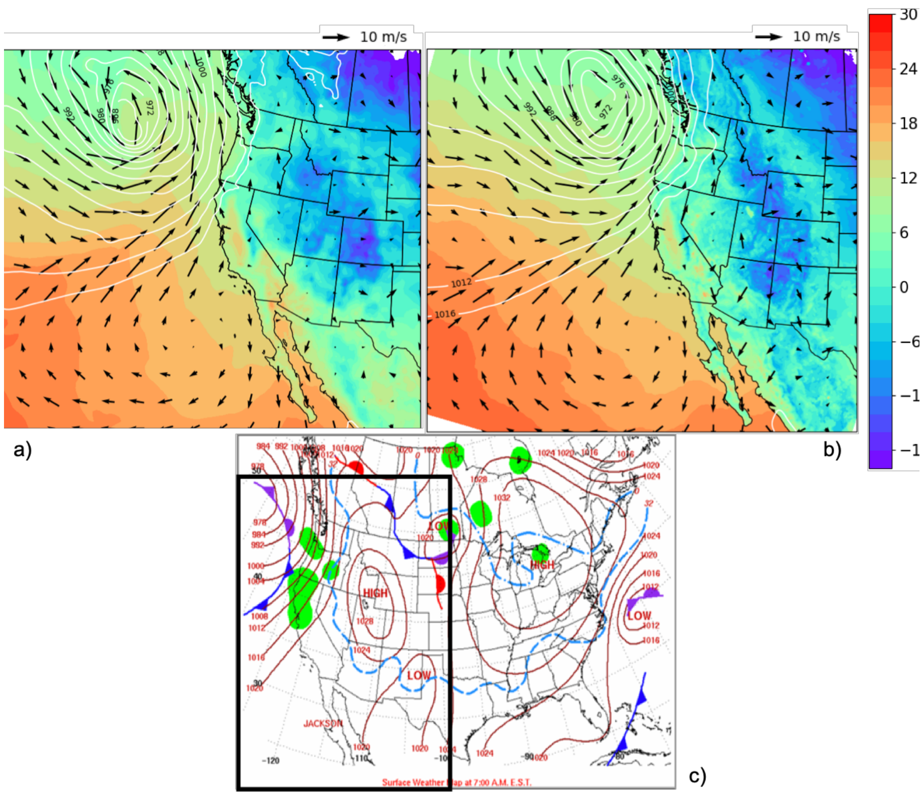

Figure 4: a,b) mean sea level pressure (mslp, white contour lines, hPa), surface temperature (color shading, °C) and 100-m wind direction (black arrows, m/s) at 0700 UTC, February 16, 2004 of ERA5 reanalysis and RegCM 12km respectively. c) NCEP-NOA Surface Analysis of pressure and fronts. The black box in c) bounded the area represented in a) and b)

The intermediate resolution (12 km) domain (Figure 3a) covers a wide area encompassing California and a large portion of the coastal Pacific Ocean, with 23 vertical levels and a parameterization for deep convection based on the Kain–Fritsch scheme (Kain, 2004). The ERA-Interim driven simulation is initialized at 0000 UTC, February 15 2004 (Table 2) and lasts until 0000 UTC February 19 2004. This simulation is used as a boundary conditions for a RegCM4-NH run over a smaller area centered over northern California (Fig. 3a) at 3 km horizontal resolution, with 41 vertical levels and boundary conditions updated every 6 hours. In RegCM4-NH only the shallow convection code of the Tiedtke scheme (Tiedtke, 1996) is activated. Simulated precipitation is compared with the CHIRPS, CMORPH, TRMM, PRISM, NCEP/CPC observations (Table 3).

As shown in Figure 4 the February 14 synoptic conditions for mean sea level pressure (mslp), surface temperature and wind direction of this case study, are well reproduced by RegCM4 at 12 km (Fig. 4b) when compared to ERA5 reanalysis (Fig. 4a). The surface analysis of pressure and fronts derived from the operational weather maps prepared at the National Centers for Environmental Prediction, Hydrometeorological Prediction Center, National Weather Service (https://www.wpc.ncep.noaa.gov/dailywxmap/index_20040216.html) is also reported in Figure 4c.

The available observed precipitation datasets show similar patterns for the total accumulated precipitation (Figure 5), in particular CHIRPS (Figure 5a), PRISM (Figure 5d) and NCEP (Figure 5e) exhibit similar spatial details and magnitudes of extremes. CHIRPS shows a maximum around 42°N which is not found in the other datasets. CMORPH (Figure 5b) and TRMM (Figure 5c) show lower precipitation maxima and lesser spatial details due to their lower resolution, indicating that the performance of satellite-

Deleted:)
Deleted:
Deleted: (
Deleted:
Deleted:)(
Deleted: :
Deleted: 16
Deleted: .
Deleted:
Deleted:
Deleted: 15
Deleted: .1
Deleted: 19
Deleted: drives a corresponding
Deleted: using a
Deleted: domain
Deleted: 2
Deleted: grid spacing
Deleted: and
Deleted: , with
Deleted: at
Deleted: intervals
Deleted: component
Deleted:
Deleted: described in
Deleted: .
Deleted: First, we notice
Deleted: that
Deleted: on 14 Feb at 7:00 am characteristic
Deleted: which are fed into the RegCM4-NH model,
Deleted: 3
Deleted: , as shown in Figure 4, where we compare the mean sea level pressure (mslp), surface temperature and wind direction on 14 Feb at 7:00 am, as simulated by RegCM at 12 km (Fig.43b) with corresponding fields from the ERA5 reanalysis (Fig.4a).
Deleted: places

based products may be insufficient as a stand alone product to validate the model for this case.

The largest observed maxima are placed on the terrain peaks, with extreme rainfall greater than 250 mm in 60 hours over the coastal mountains and between 100 – 175 mm elsewhere (Fig. 5). The black box in Fig 5a shows the area of the Russian River watershed where the largest rainfall rates were detected (269 mm and 124 mm in 60-h accumulated rainfall between 0000 UTC February 16 and 1200 UTC February 18, 2004, respectively) (Ralph et al., 2006).

The convection-permitting simulation captures the basic features of the observed precipitation both in terms of spatial distribution (Fig. 5f) and of temporal evolution of rainfall (Fig. 6a). However, it shows higher precipitation rates than observed over the sea and over the mountain chains, with lower intensities than observed in the south-east part of the mountain chain (Fig. 5). The 12-km simulation instead severely underestimates the magnitude of the event (Fig. 5g).

Figure 6a shows the 6-hourly accumulated precipitation averaged over the black box in Figure 5a. The 3 km and 12 km simulations capture the onset of the event, but the peak intensity is strongly underestimated by the 12 km run, while it is well simulated by the 3 km run, although the secondary maximum is overestimated. These results demonstrate that only the high resolution convection-permitting model is able to captures this extreme event, and that parameterized convection has severe limits in this regard (Done et al. 2004; Lean et al. 2008; Weisman et al. 2008; Weusthoff et al. 2010; Schwartz 2014; Clark et al. 2016).

Deleted: In general, the observed precipitation datasets place Tt…

Deleted: highest

Deleted: maxima

Deleted: greater

Deleted: than

Deleted: a

Deleted:

Deleted: ,

Deleted: highlighting the locations of the observing systems, including Cazadero (CZD) and Bodega Bay (BBY) where the largest rainfall rates were detected, 269 mm and 124 mm in 60-h accumulated rainfall between 0000 UTC 16 February and 1200 UTC 18 February 2004, respectively

Deleted:

Deleted: as shown for example in Fig. 5

Deleted: ,

Deleted: By contrast, t

Deleted: instead, severely

Deleted: precipitation

Deleted: Concerning the timing and intensity of the event in the CZD subregion,

Deleted:

Deleted: (Fig.6a)

Deleted: of

Deleted: shows that Bothboth

Deleted: the

Deleted: refore, our

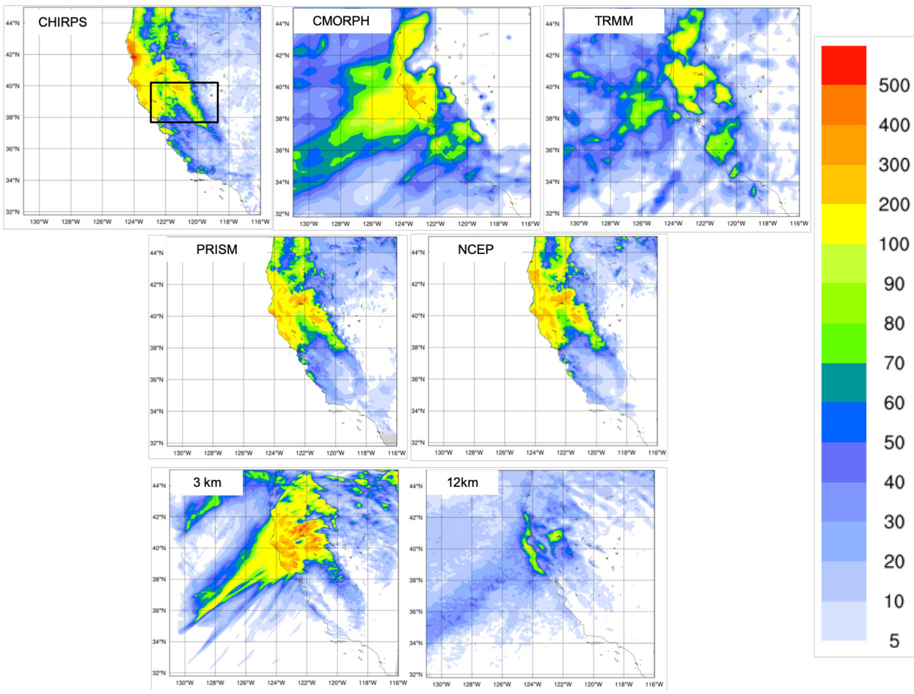

Figure 5 : Total accumulated precipitation (mm) during the California case: CHIRPS (a), CMORPH (b), TRMM (c) observations, PRISM (d) and NCEP Reanalysis (e) and convection-permitting simulation with RegCM4-NH at 3km (f) and RegCM4 at 12km (g).The black box denotes the area where the spatial average of 6-hourly accumulated precipitation is calculated and reported in Fig. 6.

Deleted: (top line)

Deleted: (middle line)

Deleted: bottom line

Deleted:

CAL (a)	TEX (b)
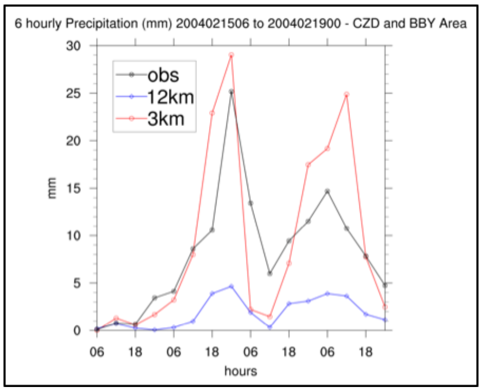	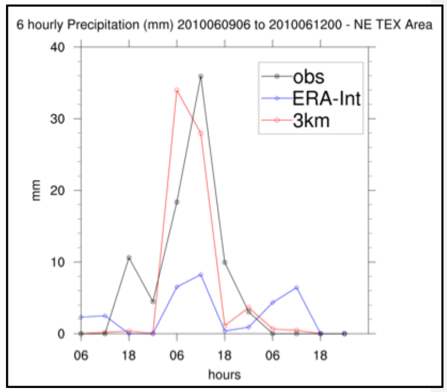

Figure 6: Time series of the 6 hourly accumulated precipitation (in mm on the y-axis) during the CAL event (a) and during the TEX event (b). The blue lines show RegCM4 12 Km and ERA interim 6 hourly accumulated precipitation averaged over the areas indicated by the black squares in Figures 5 and 7, while the red line shows the 6 hourly accumulated precipitation simulated by RegCM4-NH. The observations are shown with a black line.

Deleted: red
Deleted: 3
Deleted: (a,b)

Texas

Case 2, hereafter referred to as TEX (Table 2), is a convective precipitation episode exhibiting characteristics of the "Maya Express" flood events, linking tropical moisture plumes from the Caribbean and Gulf of Mexico to midlatitude flooding over the central United States (Higgins 2011). During the TEX event, an upper-level cutoff low over northeastern Texas, embedded within a synoptic-scale ridge, moved slowly northeastward. Strong low-level flow and moisture transport from the western Gulf of Mexico progressed northward across eastern Texas. The event was characterized by low-level moisture convergence, weak upper-level flow, weak vertical wind shear, and relatively cold air (center of cutoff low), which favored the slow-moving convective storms and nearly stationary thunderstorm outflow boundaries. The main flooding event in

Deleted: 1

eastern Texas occurred on June 10, 2010, with a daily maximum rainfall of 216.4 mm for the region in the black box of Figure 7a (Higgins 2011).

Deleted: of

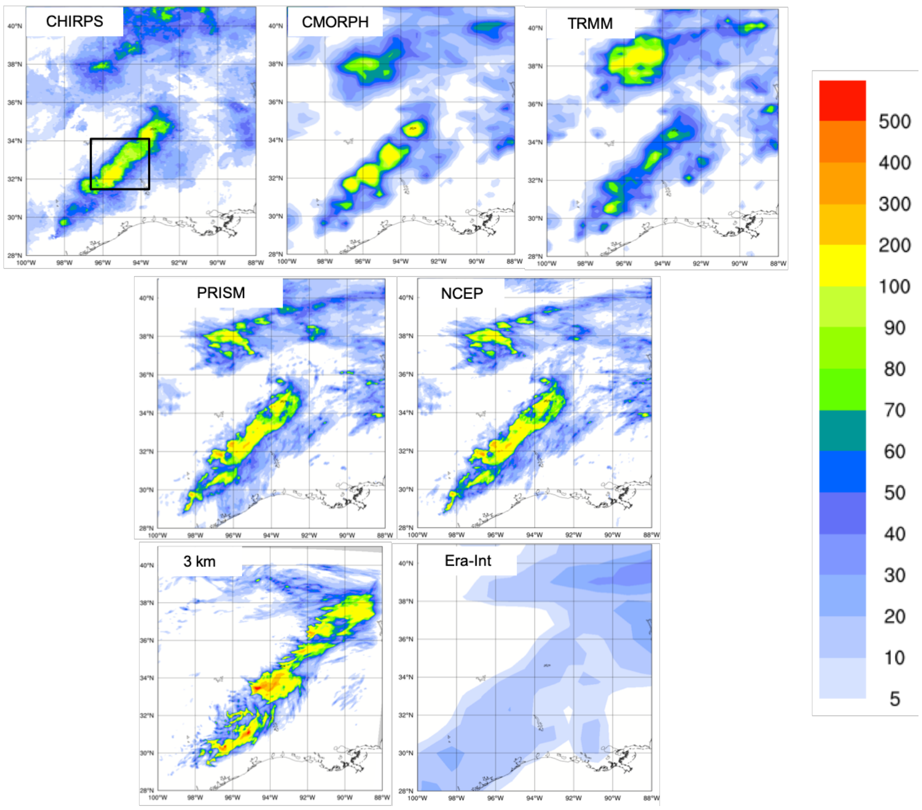

Figure 7: Total accumulated precipitation (mm) during the Texas case: CHIRPS (a), CMORPH (b), TRMM (c), PRISM (d), NCEP Reanalysis (e) and convection-permitting simulation with RegCM4-NH at 3 km grid spacing (f) and ERA-Interim (g).The black box (a) shows the area where the spatial average of 6-hourly accumulated precipitation was calculated and reported in Figure 6b

Deleted: observations (top line)

Deleted: and

Deleted: (central line)

Deleted: Era-Int

Deleted: bottom line

As for the California case, the observed precipitation datasets show coherent patterns for the total accumulated precipitation (Figure 7), with the highest values related to the mesoscale convective system in eastern Texas (~ 200 mm), and another smaller area of

Deleted: 6

high precipitation more to the north, approximately over Oklahoma. PRISM (Figure 7d) and NCEP (Figure 7e) capture similar spatial details and magnitudes of extremes, CHIRPS (Figure 7a) has lower precipitation extremes in the north compared to the other datasets, while CMORPH (Figure 7b) and TRMM (Figure 7c) show the lowest precipitation extremes and reduced spatial details as already noted for the California case.

Deleted:
Deleted:

Figure 7f and Figure 7g present precipitation as produced by the RegCM4-NH and the ERA-Interim reanalysis (driving data) respectively. ERA-Interim reproduces some of the observed features of precipitation, but with a substantial underestimation over the areas of maximum precipitation because of its coarse resolution. By comparison, the RegCM4-NH simulation (Fig. 7f) shows an improvement in both pattern and intensity of precipitation, and is substantially closer to observations over eastern Texas. However, the precipitation area is slightly overestimated and the model is not capable of reproducing the small region of maximum precipitation in the north.

Deleted: The bottom panels in
Deleted: l
Deleted:
Deleted:
Deleted: ,
Deleted: 6

The time series of precipitation over eastern Texas from June 9 to 12, 2010 for observations (black line), ERA-Interim (blue line) and RegCM4-NH (red line) are reported in figure 6b. Precipitation increases over this region from 0000 UTC until it reaches the observed maximum at 1200 UTC, on June 10 (~35 mm), gradually decreasing afterwards until 0600 UTC, on June 11. The RegCM4-NH simulation shows a more realistic temporal evolution than the ERA-Interim, which exhibits an overall underestimation of precipitation. The non-hydrostatic model produces precipitation values closer to the observations, however the simulated maximum is reached 6 hours earlier than observed.

Deleted: June
Deleted: :
Deleted: , 10 June,
Deleted: :
Deleted: June
Deleted: :
Deleted: June
Deleted: In general, t
Deleted: ,

Lake Victoria

Case 3 focuses on Lake Victoria (LKV), with the purpose of testing RegCM4-NH on a complex and challenging region in terms of convective rainfall. It is estimated that each year 3,000-5,000 fishermen perish on the lake due to nightly storms (Red Cross, 2014). In the Lake Victoria basin, the diurnal cycle of convection is strongly influenced by lake/land breezes driven by the thermal gradient between the lake surface and the surrounding land. As the land warms during the course of the day, a lake breeze is generated which flows from the relatively cooler water towards the warmer land surface. The circulation is effectively reversed at night, when the land surface becomes cooler than the lake surface, leading to convergence over the lake and associated thermal instability.

In the LKV region, prevailing winds are generally easterly most of the year with some variability due to the movement of the ITCZ. The local diurnal circulation created by the presence of the lake creates two diurnal rainfall maxima. During daylight hours, when the lake breeze begins to advance inland, convergence is maximized on the eastern coast of the lake as the lake breeze interacts with the prevailing easterlies. Studies have also noted the importance of downslope katabatic winds along the mountains to the east of the lake in facilitating convergence along the eastern coastal regions (Anyah et al. 2006). This creates a maximum in rainfall and convection on the eastern coast of LKV. Conversely, during nighttime hours, when the local lake circulation switches to flow from the land towards the lake, the prevailing easterlies create locally strong easterly flow across the lake and an associated maximum in convergence and rainfall on the western side of LKV.

Deleted: within the larger scale easterly wind field

The LKV simulation starts on November 25, 1999 and extends to the beginning of December 1999 (Table 2), covering a 5-day period which falls within the short-rain season of East Africa. The choice of 1999, an ENSO neutral year, was made in order to focus the analysis on local effects, such as the diurnal convection cycle in response to the lake/land breeze, with no influence of anomalous large scale conditions. A 1-dimensional lake model (Hostetler et al. 1993; Bennington et al. 2014) interactively coupled to RegCM4-NH was utilized to calculate the lake surface temperature (LST), since lake-atmosphere coupling has been shown to be important for LKV (Sun et al. 2015; Song et al. 2004). This coupled lake model has been already used for other lakes, including Lake Malawi in southern Africa (Diallo et al. 2018). As with the other experiments, the boundary conditions are provided by a corresponding 12 km RegCM4 simulation employing the convection scheme of Tiedtke (1996).

Deleted: 25

Deleted: the

At the beginning of the simulation, the LST over the lake is uniformly set to 26°C, and is then allowed to evolve according to the lake-atmosphere coupling. This initial LST value is based on previous studies. For example, Talling (1969) finds Lake Victoria surface temperatures ranging from 24.5-26°C during the course of the year. Several studies have used RCMs to investigate the Lake Victoria climate (Anya et al., 2006; Anyah and Semazzi 2009, Sun et al. 2015), and found a significant relationship between lake temperature and rainfall depending on season. The value of 26°C is typical of the winter season and was chosen based on preliminary sensitivity tests using different values of initial temperature ranging from 24°C to 26°C.

The synoptic feature favorable for the production of precipitation over the LKV in this period corresponds to a large area of southeasterly flow from the Indian Ocean (Fig. 8a), which brings low-level warm moist air into the LKV region facilitating the production of convective instability and precipitation. This synoptic situation, with a low-level south-easterly jet off the Indian Ocean, is a common feature associated with high precipitation in the area (Anyah et al. 2006), and can be seen in ERA5 data (Figure 8a). Although some bias in terms of magnitude, this is reasonably well reproduce by the 12 km simulation (Figure 8b).

Deleted:

Deleted: is found

Deleted: 7

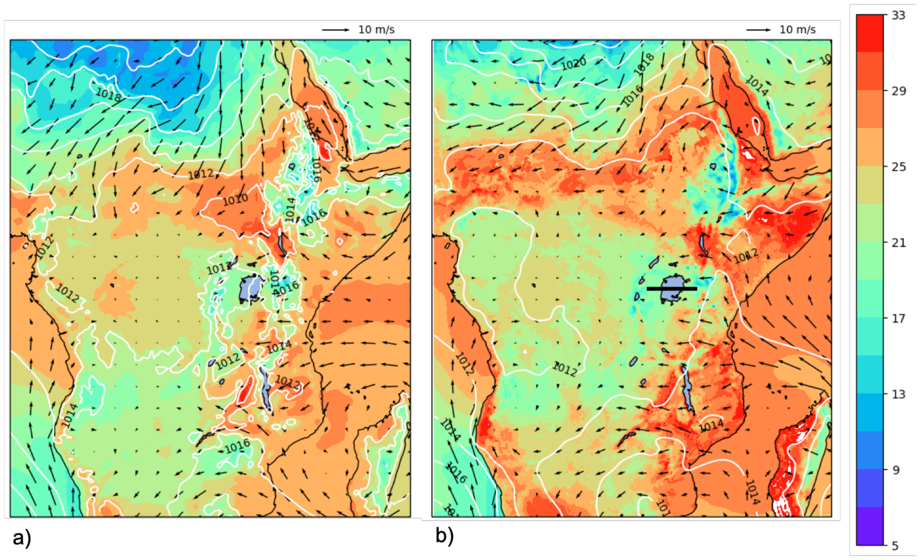

Figure 8: Mean sea level pressure (mslp) (hPa) (white contour lines), surface temperature (color shading) (°C) and 100-m wind (black arrows) averaged over the period 25 November 0000 UTC - 1 December 0000 UTC, by ERA5 reanalysis (a) and RegCM 12km (b). The black line (b) shows the cross-section position represented in Fig. 9

The LKV region dynamics are quite distinct between nighttime and daytime and the rainfall in and around the lake has a pronounced diurnal cycle. To understand this strong diurnal cycle, Figure 9 shows a cross-section through the lake (32°E to 34°E, black line in right panel of Fig. 8b) along 1°S latitude at a period during strong nighttime (Fig. 9b,d; 0600Z November 30) and daytime convection (Figure 9a,c; 12Z November 29). Wind vectors in Figure 9 show the zonal-wind anomaly across 0°-2°S to highlight the circulations associated with LKV. During the day, surface heating around the lake leads to a temperature difference between the land and lake sufficient to generate a lake breeze, which causes divergence over the lake, while over the highlands to the east the environment is more conducive to convection where convergence is focused (9a,c). Conversely, during the night, a land breeze circulation is generated, which induces convergence and convection over the lake (Figure 9b,d). In Figure 10, the evolution of

Deleted: black
Deleted: direction
Deleted:
Deleted: :
Deleted: :
Deleted: of
Deleted: .
Deleted: 7
Deleted: o
Deleted: 30
Deleted: .
Deleted: 29
Deleted: tial
Deleted: surrounding
Deleted:
Deleted: .

the nighttime land breeze is illustrated with cooler temperature anomalies propagating westward onto the lake during the night.

Comparing the 3 km simulation to the 12 km forcing run, we find that the localized circulations created by local forcings (i.e. convection) are much stronger in the convection permitting resolution experiment. We also find stronger and more localized areas of convective updrafts compared to the 12 km simulation (Figure 9c,d; omega is shown instead of vertical velocity here because of the difference in dynamical core). As an example during the nighttime event (Figure 9b,d), there is a broad area of upward motion over the lake and the associated broad convergence in the 12km simulation, while in the convection permitting 3km simulation, convection is much more local and concentrated over the western part of the lake. Indeed, nighttime rainfall tends to be concentrated over the western part of the lake (Sun et al. 2015; Figure 11a-d). Stronger convection simulated in the 3 km experiment could also be tied to stronger temperature anomalies shown over the lake and land and between day and night relative to the 12km simulation (Figure 10). The 3km simulation also shows a more pronounced land breeze propagation at night compared to the 12km simulation.

This demonstrates that the 3km simulation is better equipped to simulate the localized circulations associated with this complex land-lake system.

Deleted: high resolution

Deleted: as seen in the vertical velocities (9a,b)

Deleted: 8

Deleted: model output

Deleted: For example Forfor

Deleted: .

Deleted: note the

Deleted: .

Deleted: The s

Deleted: is

Deleted: the

Deleted: gradients between

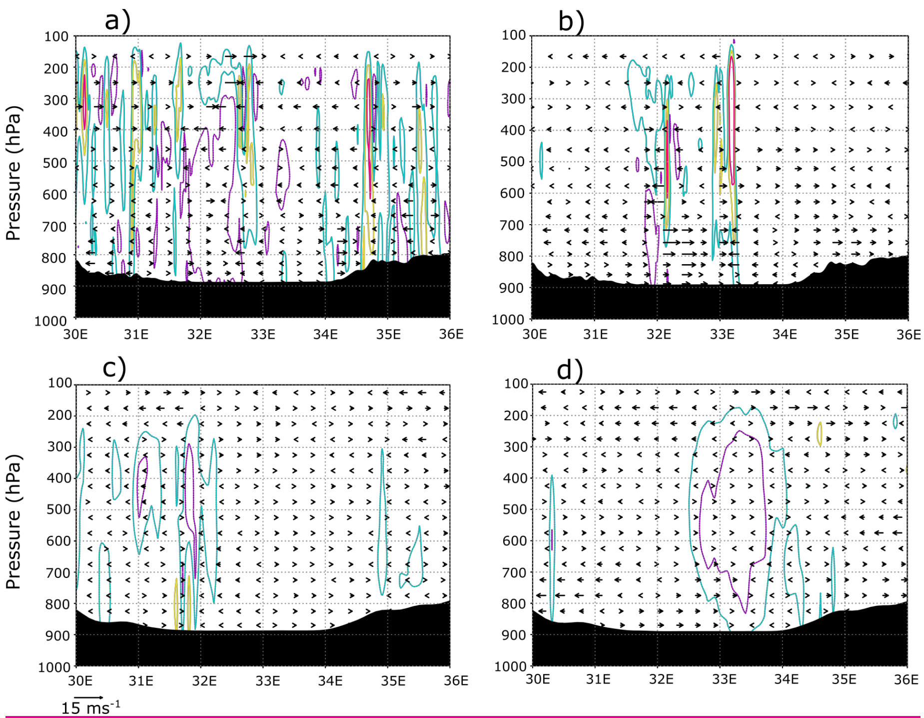

Figure 9. Cross-section through 1ºS (black line in Fig. 8b) of the zonal-wind anomaly (0o-2oS) vectors and the mean contoured vertical velocity (m/s) over 0°-2°S at a) 12Z 29 November and b) 6Z 30 November from the 3km simulation. Purple dashed contours indicate -0.1 m/s, light blue contours indicate 0.1 m/s, yellow contours indicate 0.3 m/s, and red contours indicate 0.5 m/s. Lake Victoria encompasses about 32°E to 34°E. The bottom 2 panels show the same as in a) and b) but from the 12km simulation at c) 12Z 29 November and d) 6Z 30 November. Purple dashed contours indicate -0.01 hPa/s, light blue dashed contours indicate -0.005 hPa/s, and yellow dashed contours indicate 0.005 hPa/s.

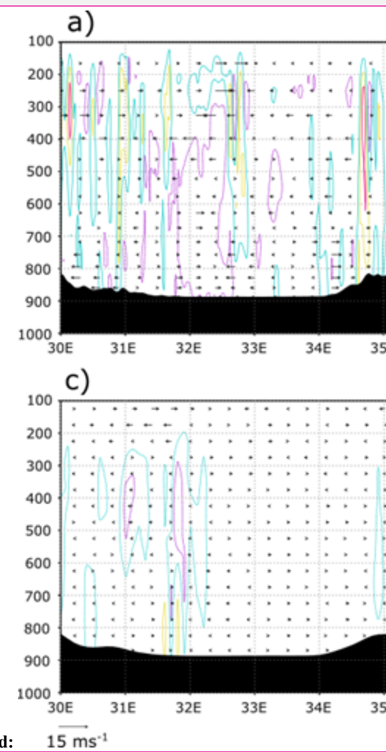

Deleted: 15 ms-1

Deleted: red

Deleted: bottom right panel of

Deleted: 9

Deleted: mean (0º-2ºN)

Deleted: (30°E-36°E)

Deleted: 0o-2oS

Deleted: cross-section also through 1ºS and mean zonal-wind anomaly vectors

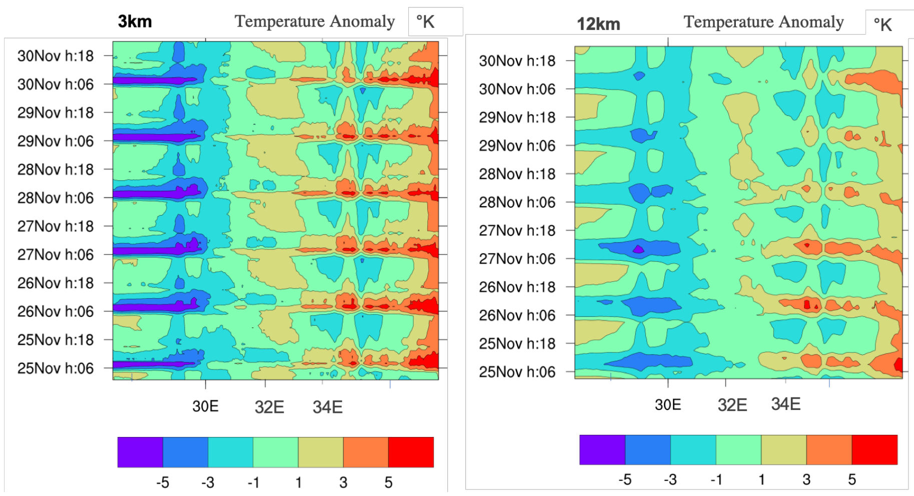

Figure 10 : Longitude-time (hourly) Hovmöller diagram of LKV domain surface temperature anomaly (shading, in °K). Panels correspond to the 3km simulation (left) and 12km simulation (right). The lake Victoria is between 32°E and 34°E longitude

Deleted: C

Deleted:

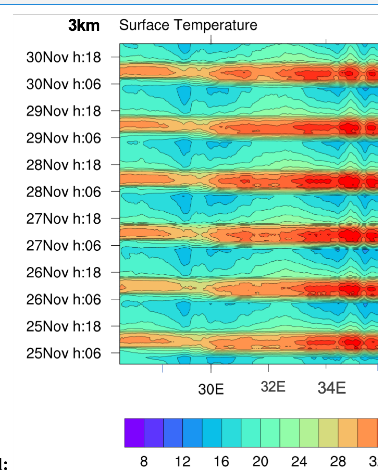

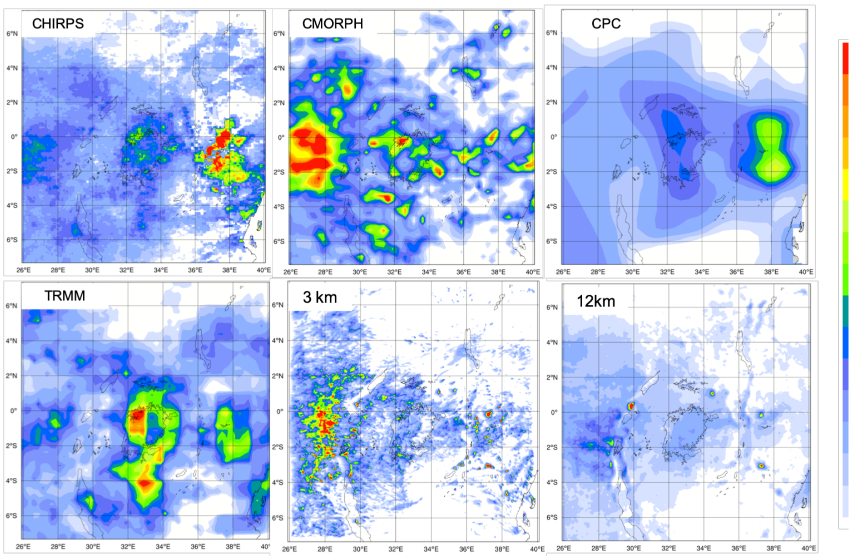

Figure 11: Total event accumulated precipitation (mm) during the LKV case (Nov.ember 25, 1999-December 1, 1999) measured by CHIRPS (a), CMORPH (b), CPC (d) TRMM (e) and calculated by RegCM4 at 3 km (e) and 12 km (f).

Figure 11 reports the total accumulated precipitation observed and simulated for the LKV case. TRMM (Figure 11d) and CPC (Figure 11c) show a similar pattern, with two-rainfall maxima of different intensities over the southeastern and northwestern lake areas. CMORPH (Figure 11b) shows a western rainfall maximum similar to TRMM and one large rainfall area almost entirely centered over the highlands to the west of the lake. Conversely in CHIRPS (Figure 11a) a maximum is found to the east of the lake while several localized maxima occur over the lake. The differences among the observed datasets highlight the issue of observational uncertainty and the need to take into consideration shortcomings associated with the types of observational datasets considered. Different datasets can have significantly different climatologies, especially in areas of low data availability. For example, Prein and Gobiet (2017) analyzed two gauge-based European-wide datasets, and seven global low-resolution datasets, and found

Deleted:
Deleted: top left
Deleted: top center
Deleted: (top right)
Deleted: bottom left
Deleted: bottom center
Deleted: bottom right
Deleted:
Deleted: finally
Deleted:
Deleted:
Deleted: between
Deleted:
Deleted: y
Deleted:

large differences across the observation products, often of similar magnitude as the difference among model simulations. In this case and for this area the observation uncertainty plays a big role especially at high resolution, and highlights the need for an adequate observational network for model validation. However, despite the large uncertainty among the different observed datasets (Figure 11 a-d), we find a significant underestimation of the precipitation by the 12 km run over the lake independently of the dataset used as a reference (Figure11f). In contrast, the 3 km simulation (Figure 11e) shows substantially greater detail, with rainfall patterns more in agreement with the CMORPH data. In particular, the 3 km simulation reproduces well the local rainfall maxima on the western side of the lake, although these appear more localized and with a multi-cell structure compared to CMORPH and TRMM. Additionally, the 12 km simulation underestimates the observed heavy rainfall totals in the highlands to the west of the lake region especially when compared to CMORPH, which are instead reproduced by the 3 km simulation.

This last test case demonstrates the ability of RegCM4-NH in simulating realistic convective activity over a such morphologically complex region, which is a significant improvement compared to the hydrostatic-coarse resolution model configuration.

Conclusions and future outlook

In this paper we have described the development of RegCM4-NH, a non hydrostatic version of the regional model system RegCM4, which was completed in response to the need of moving to simulations at convection-permitting resolutions of a few kilometers. The non-hydrostatic dynamical core of MM5 has been incorporated into the RegCM4 system previously based on the MM5 hydrostatic core. Some modifications to the MM5 dynamical core were also implemented to increase the model stability for long term runs. RegCM4-NH also includes two explicit cloud microphysics schemes needed to explicitly describe convection and cloud processes in the absence of the use of cumulus convection schemes. Finally, we presented a few case studies of explosive convection to

Deleted: between

Deleted: .

Deleted:

Deleted:

Deleted: ¶

Deleted: However, even taking into account the elevated uncertainty existing in the observations datasets, we find a significant underestimation of rain amounts in the 12 km run¶

Deleted:

Deleted: compared to any of them

Deleted:

Deleted:

Deleted: 0

Deleted: , with a wide area of rainfall around 80mm over the whole of LKV…

Deleted:

Deleted: .

Deleted:

Deleted:

Deleted: m

Deleted: the non-hydrostatic version of

Deleted: thus

Deleted: , an approach facilitated by the fact that the this last is essentially an evolution of the MM5.

illustrate how the model provides realistic results in different settings and general improvements compared to the coarser resolution hydrostatic version of RegCM4 for such types of events.

As already mentioned, RegCM4-NH is currently being used for different projects, and within these contests, is being run at grid spacings of a few kilometers for continuous decadal simulations, driven by reanalyses of observations or GCM boundary conditions (with the use of an intermediate resolution domains) over different regions, such as the Alps, the Eastern Mediterranean, Central-Eastern Europe and the Caribbeans. These projects, involving multi-model intercomparisons, indicate that the performance of RegCM4-NH is generally in line with that of other convection-permitting models, and exhibits similar improvements compared to coarser resolution models, such as a better simulation of the precipitation diurnal cycle and of extremes at hourly to daily time scales. The results obtained within the multi-model context confirm previous results from single-model studies (Kendon et al. 2012, 2017, Ban et al. 2014, 2015; Prein et al. 2015, 2017), but also strengthen the robustness of the findings through reduced uncertainty compared to coarse resolution counterpart (Ban et al., 2021, Pichelli et al., 2021). The convection-permitting scale can thus open the perspective of more robust projections of future changes of precipitation, especially over sub-daily time scales.

Deleted: km

Deleted:

Deleted:

Deleted:

Deleted: short

One of the problems of the RegCM4-NH dynamical core is that, especially for long runs with varied meteorological conditions, a relatively short time step is needed for stability reasons. This makes the model rather computationally demanding, although not more than other convection-permitting modeling systems such as the Weather Research and Forecast model (WRF, Skamarok et al. 2008). For this reason, we are currently incorporating within the RegCM system a very different and more computationally efficient non-hydrostatic dynamical core, which will provide the basis for the next version of the model, RegCM5, to be released in the future.

Deleted: s

Deleted: to be used

Following the philosophy of the RegCM modeling system, RegCM4-NH is intended to be a public, free, open source community resource for external model users. The non-hydrostatic dynamical core has been implemented in a way that it can be activated in place of the hydrostatic dynamics through a user-set switch, which makes the use of RegCM4-NH particularly simple and flexible. We therefore envision that the model will be increasingly used by a broad community so that a better understanding can be achieved of its behavior, advantages and limitations.

Code availability: https://zenodo.org/record/4603556
Cases study configuration files: https://zenodo.org/record/5106399

Author contribution: CE prepared the manuscript with contributions from all co-authors and coordinated research, SP, TA, GR carried out and analysed the simulations, PE investigated solutions to stabilize/adapt the model at the km-scale and performed preliminary validation tests, GG developed/adapted the model code, FDS contributed to develop the coupled version of the model, NR developed one of the microphysics scheme, GF supervised and coordinated all activities.

Competing interests: The authors declare that they have no conflict of interest.

References

Anyah, R., Semazzi, F. H. M., Xie, L., 2006: Simulated Physical Mechanisms Associated with Climate Variability over Lake Victoria Basin in East Africa, Mon. Wea. Rev., 134 3588-3609.

Anthes, R. A., Hsie, E. -Y., & Kuo, Y. -H. (1987). Description of the Penn State/NCAR Mesoscale Model: Version 4 (MM4) (No. NCAR/TN-282+STR). doi:10.5065/D64B2Z90

Anyah, R. O., F. H. M. Semazzi, L. Xie, 2006: Simulated Physical Mechanisms Associated with Climate Variability over Lake Victoria Basin in East Africa. Mon. Wea. Rev., 134, 3588-3609,.

Anyah RO, Semazzi F (2009) Idealized simulation of hydrodynamic characteristics of Lake Victoria that potentially modulate regional climate. Int J Climatol 29(7):971–981. doi:10.1002/joc.1795

Ashouri, Hamed, Kuo Lin Hsu, Soroosh Sorooshian, Dan K. Braithwaite, Kenneth R. Knapp, L. Dewayne Cecil, Brian R. Nelson and Olivier P. Prat (2015). 'PERSIANN- CDR: Daily precipitation climate data record from multisatellite observations for hydrological and climate studies'. In: *Bulletin of the American Meteorological Society*. ISSN: 00030007. DOI: 10.1175/BAMS-D-13-00068.1.

Ban, N., J. Schmidli, and C. Schär, 2014: Evaluation of the convection-resolving regional climate modeling approach in decade-long simulations. J. Geophys. Res. Atmos., 119, 7889– 7907, https://doi.org/10.1002/2014JD021478.

Ban N, Schmidli J, Schär C (2015) Heavy precipitation in a changing climate: does short-term summer precipitation increase faster? Geophys Res Lett 42:1165–1172. https://doi.org/10.1002/2014G L062588

Ban, N., Caillaud, C., Coppola, E. *et al.* The first multi-model ensemble of regional climate simulations at kilometer-scale resolution, part I: evaluation of precipitation. *Clim Dyn* (2021). https://doi.org/10.1007/s00382-021-05708-w

Beheng, K.: A parameterization of warm cloud microphysical conversion processes, Atmos. Res., 33, 193–206, 1994

Bennington V, Notaro M, Holman KD, 2014: Improving Climate Sensitivity of Deep Lakes within a Regional Climate Model and Its Impact on Simulated Climate, J. Climl, 27, 2886-2911.

Bretherton CS, McCaa JR, Grenier H (2004) A new parame-terization for shallow cumulus convection and its appli-cation to marine subtropical cloud-topped boundary lay-ers. I. Description and 1D results. Mon Weather Rev 132: 864– 882

Chan, S. C., E. J. Kendon, H. J. Fowler, S. Blenkinsop, N. M. Roberts, and C. A. T. Ferro, 2014: The value of high- resolution Met Office regional climate models in the simula- tion of multi-hourly precipitation extremes. J. Climate, 27, 6155–6174, https://doi.org/10.1175/JCLI-D-13-00723.1.

Chen, Mingyue and Pingping Xie (2008). 'CPC Unified Gauge-based Analysis of Global Daily Precipitation'. In: *2008 Western Pacific Geophysics Meeting*. ISBN: 0026- 0576. DOI: http://dx.doi.org/10.1016/S0026-0576(07)80022-5.

Clark, P., N. Roberts, H. Lean, S. P. Ballard, and C. Charlton- Perez, 2016: Convection-permitting models: A step-change in rainfall forecasting. Meteor. Appl., 23, 165–181, https://doi.org/ 10.1002/met.1538.

Coppola, E., Sobolowski, S., Pichelli, E. et al. A first-of-its-kind multi-model convection permitting ensemble for investigating convective phenomena over Europe and the Mediterranean. Clim Dyn 55, 3–34 (2020). https://doi.org/10.1007/s00382-018-4521-8

Coppola E, Giorgi F, Mariotti L, Bi X (2012) RegT-Band: a tropical band version of RegCM4. Clim Res 52: 115–133

Dacre, H. F., P. A. Clark, O. Martinez-Alvarado, M. A. Stringer, and D. A. Lavers, 2015: How do atmospheric rivers form? Bull. Amer. Meteor. Soc., 96, 1243-1255, https://doi.org/10.1175/BAMS-D-14-00031.

Dale, M., A. Hosking, E. Gill, E. J. Kendon, H. J. Fowler, S. Blenkinsop, and S. C. Chan, 2018: Understanding how changing rainfall may impact on urban drainage systems; lessons from projects in the UK and USA. Water Pract. Technol., 13, 654–661, https://doi.org/10.2166/wpt.2018.069.

Diallo, I., Giorgi, F. and Stordal, F. (2018) Influence of Lake Malawi on regional climate from a double nested regional climate model experiment. Climate Dynamics, 50, 3397–3411. https://doi.org/10.1007/s00382-017-3811-x

Dickinson, R.E., Errico, R.M., Giorgi, F. et al. A regional climate model for the western United States. Climatic Change 15, 383–422 (1989). https://doi.org/10.1007/BF00240465

Dickinson RE, Henderson-Sellers A, Kennedy P (1993) Bio -sphere– atmosphere transfer scheme (BATS) version 1eas coupled to the NCAR community climate model. TechRep, National Center for Atmospheric Research TechNote NCAR.TN-387+ STR, NCAR, Boulder, CO

Done, J., C. A. Davis, and M. L. Weisman, 2004: The next gener- ation of NWP: Explicit forecasts of convection using the Weather Research and Forecasting (WRF) model. Atmos. Sci. Lett., 5, 110–117, https://doi.org/10.1002/asl.72.

Dudhia, J., 1989: Numerical study of convection observed during the winter monsoon experiment using a mesoscale two-dimensional model, J. Atmos. Sci., 46, 3077–3107.

Durran D.R. and Klemp J.B.: A compressible model for the simulation of moist mountain waves, Mon. Wea. Rev., 111, 2341–236, 1983.

Elguindi N., Bi X., Giorgi F. , Nagarajan, B. Pal J., Solmon F., Rauscher S., Zakey S., O'Brien T., Nogherotto R. and Giuliani G., 2017: Regional Climate Model RegCMReference ManualVersion 4.7, 49 pp, https://zenodo.org/record/4603616

Emanuel KA (1991) A scheme for representing cumulus convection in large-scale models. J Atmos Sci 48:2313–2335

Fairall, C.W., E.F. Bradley, J.S. Godfrey, G.A. Wick, J.B. Edson, and G.S. Young, 1996a: The cool skin and the warm layer in bulk flux calculations. *J. Geophys. Res.* 101, 1295-1308.

Fairall, C.W., E.F. Bradley, D.P. Rogers, J.B. Edson, G.S. Young, 1996b: Bulk parameterization of air-sea fluxes for TOGA COARE. *J. Geophys. Res.* 101, 3747-3764

Funk, C., Peterson, P., Landsfeld, M. et al. The climate hazards infrared precipitation with stations—a new environmental record for monitoring extremes. Sci Data 2, 150066 (2015). https://doi.org/10.1038/sdata.2015.66

Gimeno, L., R. Nieto, M. Vàsquez, and D. A. Lavers, 2014: Atmospheric rivers: A mini-review. Front. Earth Sci., 2, https://doi.org/10.3389/feart.2014.00002.

Giorgi F (2019) Thirty years of regional climate modeling: where are we and where are we going next? J Geophys Res Atmos 124:5696–5723

Giorgi F, Coppola E, Solmon F, Mariotti L and others (2012) RegCM4: model description and preliminary tests over multiple CORDEX domains. Clim Res 52:7-29. https://doi.org/10.3354/cr01018

Giorgi F, Francisco R, Pal JS (2003) Effects of a sub-gridscale topography and landuse scheme on surface climateand hydrology. I. Effects of temperature and water vapordisaggregation. J Hydrometeorol 4: 317– 333

Giorgi F, Jones C, Asrar G (2009) Addressing climate information needs at the regional level: the CORDEX framework. WMO Bull 175–183

Giorgi F, Mearns LO (1999) Introduction to special section: regional climate modeling revisited. J Geophys Res 104:6335–6352

Giorgi F, Marinucci MR, Bates G (1993a) Development of a second generation regional climate model (RegCM2). I. Boundary layer and radiative transfer processes. MonWeather Rev 121: 2794–2813

Giorgi F, Marinucci MR, Bates G, DeCanio G (1993b) Development of a second generation regional climate model (RegCM2), part II: convective processes and assimilation of lateral boundary conditions. Mon Weather Rev 121:2814–2832

Giorgi, F., and G. T. Bates, 1989: The Climatological Skill of a Regional Model over Complex Terrain. Mon. Wea. Rev., 117, 2325–2347, https://doi.org/10.1175/1520-0493(1989)117<2325:TCSOAR>2.0.CO;2.
G. A. Grell, J. Dudhia and D. R. Stauffer, “A Description of the Fifth Generation Penn State/NCAR Mesoscale Model (MM5),” NCAR Tech. Note, NCAR/TN-398+ STR, Boulder, 1995, p. 122.

Grell GA (1993) Prognostic evaluation of assumptions usedby cumulus parameterizations. Mon Weather Rev 121: 764– 787

Grell, G., A.J. Dudhia, and D.R. Stauffer, 1994, A description of the fifth-generation Penn State/NCAR mesoscale model (MM5). NCAR Technical Note, NCAR/TN- 398+STR.

Gunn, K. L. S., and J. S. Marshall, 1958: The distribution with size of aggregate snowflakes. J. Meteor., 15, 452–461, https://doi.org/10.1175/1520-0469(1958)015<0452:TDWSOA>2.0.CO;2.

Gutowski Jr., W. J., Giorgi, F., Timbal, B., Frigon, A., Jacob, D., Kang, H.-S., Raghavan, K., Lee, B., Lennard, C., Nikulin, G., O'Rourke, E., Rixen, M., Solman, S., Stephenson, T., and Tangang, F.: WCRP COordinated Regional Downscaling EXperiment (CORDEX):

a diagnostic MIP for CMIP6, Geosci. Model Dev., 9, 4087–4095, https://doi.org/10.5194/gmd-9-4087-2016, 2016

Holtslag A, de Bruijn E, Pan HL (1990) A high resolution air mass transformation model for short-range weather fore-casting. Mon Weather Rev 118: 1561–1575

Hostetler SW, Bates GT, Giorgi F (1993) Interactive nesting of a lake thermal model within a regional climate model for climate change studies. J Geophys Res 98: 5045– 5057

Huffman, G. J., and Coauthors, 2007: The TRMM Multisatellite Precipitation Analysis (TMPA): Quasi-global, multiyear, combined-sensor precipitation estimates at fine scales. J. Hydrometeor., 8, 38–55, doi:https://doi.org/10.1175/JHM560.1

Kiehl J, Hack J, Bonan G, Boville B, Breigleb B, WilliamsonD, Rasch P (1996) Description of the NCAR Commun -ity Climate Model (CCM3). National Center for Atmo spheric Research Tech Note NCAR/TN-420+ STR, NCAR,Boulder, CO

Lean, H. W., P. A. Clark, M. Dixon, N. M. Roberts, A. Fitch, R. Forbes, and C. Halliwell, 2008: Characteristics of high- resolution versions of the Met Office Unified Model for forecasting convection over the United Kingdom. Mon. Wea. Rev., 136, 3408–3424, https://doi.org/10.1175/2008MWR2332.1.

Lind, P., D. Lindstedt, E. Kjellstrom, and C. Jones, 2016: Spatial and temporal characteristics of summer precipitation over central Europe in a suite of high-resolution climate models. J. Climate, 29, 3501–3518, https://doi.org/10.1175/JCLI-D-15- 0463.1.

Hewitt, C. D., and J. A. Lowe, 2018: Toward a European climate prediction system. Bull. Amer. Meteor. Soc., 99, 1997–2001, https://doi.org/10.1175/BAMS-D-18-0022.1.

Hong, S.-Y., H.-M. H. Juang, and Q. Zhao, 1998: Implementation of prognostic cloud scheme for a regional spectral model, Mon. Wea. Rev., 126, 2621–2639.

Hong, S.-Y., J. Dudhia, and S.-H. Chen, 2004: A Revised Approach to Ice Microphysical Processes for the Bulk Parameterization of Clouds and Precipitation, Mon. Wea. Rev., 132, 103–120.

Hong, S.-Y., and J.-O. J. Lim, 2006: The WRF Single-Moment 6-Class Microphysics Scheme (WSM6), J. Korean Meteor. Soc., 42, 129–151

Hostetler SW, Bates GT, Giorgi F, 1993: Interactive Coupling of Lake Thermal Model with a Regional climate Model, J. Geophys. Res., 98(D3), 5045-5057.

Huffman, George J., David T. Bolvin, Eric J. Nelkin, David B. Wolff, Robert F. Adler, Guojun Gu, Yang Hong, Kenneth P. Bowman and Erich F. Stocker (2007). *The TRMM Multisatellite Precipitation Analysis (TMPA): Quasi-Global, Multiyear, Combined-Sensor Precipitation Estimates at Fine Scales*. DOI: 10.1175/JHM560.1.

Joyce, Robert J., John E. Janowiak, Phillip A. Arkin, Pingping Xie, 2004: CMORPH: A Method that Produces Global Precipitation Estimates from Passive Microwave and Infrared Data at High Spatial and Temporal Resolution. J. Hydrometeor, 5, 487–503

Kain, J. S., 2004: The Kain–Fritsch convective parameterization: An update. J. Appl. Meteor., 43, 170–181, https://doi.org/10.1175/1520-0450(2004)043<0170:TKCPAU>2.0.CO;2.

Kain, J. S., and J. M. Fritsch, 1990: A one-dimensional entraining/ detraining plume model and its application in convective parameterization, J. Atmos. Sci., 47, 2784–2802.

Kendon, E. J., N. M. Roberts, C. A. Senior, and M. J. Roberts, 2012: Realism of rainfall in a very high-resolution regional climate model. J. Climate, 25, 5791–5806, https://doi.org/ 10.1175/JCLI-D-11-00562.1.

Kendon, E. J., and Coauthors, 2017: Do convection-permitting regional climate models improve projections of future precipitation change? Bull. Amer. Meteor. Soc., 98, 79–93, https://doi.org/ 10.1175/BAMS-D-15-0004.1

Kessler, E., 1969: On the Distribution and Continuity of Water Substance in Atmospheric Circulations. Meteor. Monogr., No. 32, Amer. Meteor. Soc., 84 pp.

Khairoutdinov, M. and Kogan, Y.: A new cloud physics parameterization in a large-eddy simulation model of marine stratocumulus, B. Am. Meteorol. Soc., 128, 229–243, 2000

Klemp, J.B. and Dudhia, J.: An Upper Gravity-Wave Absorbing Layer for NWP Applications, Monthly Weather Review, 176, 3987-4004, 2008.

Klemp, J. B. and D. K. Lilly: Numerical simulation of hydrostatic mountain waves, J. Atmos. Sci., 35, 78–107, 1978.

Lin, Y., Farley, R., and Orville, H.: Bulk parameterization of the snow field in a cloud model, J. Appl. Meteor. Clim., 22, 1065–1092, 1983.

Marshall, J. S., and W. McK. Palmer, 1948: The distribution of raindrops with size. J. Meteor., 5, 165–166.

Matte, Dominic; Laprise, René; Thériault, Julie M.; Lucas-Picher, Philippe (2017). *Spatial spin-up of fine scales in a regional climate model simulation driven by low-resolution boundary conditions. Climate Dynamics, 49(1-2), 563–574.* doi:10.1007/s00382-016-3358-2

Mlawer, E. J., S. J. Taubman, P. D. Brown, M. J. Iacono, and S. A. Clough, 1997: Radiative transfer for inhomogeneous atmospheres: RRTM, a validated correlated-k model for the longwave. J. Geophys. Res., 102, 16,663-16,682

Nogherotto, R., Tompkins, A.M., Giuliani, G., Coppola, E. and Giorgi, F.: Numerical framework and performance of the new multiple-phase cloud microphysics scheme in RegCM4. 5: precipitation, cloud microphysics, and cloud radiative effects. Geoscientific Model Development, 9(7), 2533-2547, 2016

Oleson, K. W., Lawrence, D. M., Bonan, G. B., Drewniak, B., Huang, M., Koven, C. D., Levis, S., Li, F., Riley, W. J., Subin, Z. M., Swenson, S. C., Thornton, P. E., Bozbiyik, A., Fisher, R., Kluzek, E., Lamarque, J. -F., Lawrence, P. J., Leung, L. R., Lipscomb, W., Muszala, S., Ricciuto, D. M., Sacks, W., Sun, Y., Tang, J., and Yang, Z. -L:Technical Description of version 4.5 of the Community Land Model (CLM),Ncar Technical Note NCAR/TN-503+STR, National Center for Atmospheric Research, Boulder, CO, 422 pp, DOI: 10.5065/D6RR1W7M, 2013.

Pal JS, Small E, Eltahir E (2000) Simulation of regional-scale water and energy budgets: representation of subgrid cloud and precipitation processes within RegCM. J Geo-phys Res 105: 29579–29594

Pal JS et al (2007) The ICTP RegCM3 and RegCNET: regional climate modeling for the developing world. Bull Am Meteorol Soc 88:1395–1409

Pichelli, E., Coppola, E., Sobolowski, S. *et al.* The first multi-model ensemble of regional climate simulations at kilometer-scale resolution part 2: historical and future simulations of precipitation. *Clim Dyn* (2021). https://doi.org/10.1007/s00382-021-05657-4

Prein, Andreas F. and Andreas Gobiet (2017). ‘Impacts of uncertainties in European gridded precipitation observations on regional climate analysis’. In: *International Journal of Climatology*. ISSN: 10970088. DOI: 10.1002/joc.4706

Prein, A. F. et al. A review on regional convection-permitting climate modeling: demonstrations, prospects, and challenges. Rev. Geophys. 53, 323–361 (2015).

Ralph, F. M., P. J.Neiman, G. A.Wick, S. I.Gutman, M. D.Dettinger, D. R.Cayan, and A. B.White, 2006: Flooding on California's Russian River: Role of atmospheric rivers. Geophys. Res. Lett., 33, L13801, https://doi.org/10.1029/2006GL026689

Ralph, F. M., M. D. Dettinger, M. M. Cairns, T. J. Galarneau, and J. Eylander, 2018: Defining "atmospheric river": How the Glossary of Meteorology helped resolve a debate. Bull. Amer. Meteor. Soc., 99, 837–839, https://doi.org/10.1175/BAMS-D-17-0157.1

Rutledge, S. A., and P. V. Hobbs, 1983: The mesoscale and microscale structure and organization of clouds and precipitation in midlatitude cyclones. Part VIII: A model for the ''seeder-feeder'' process in warm-frontal rainbands. J. Atmos. Sci., 40, 1185–1206.

Skamarock WC, Klemp JB, Dudhia J, Gill DO, Barker DM, Duda MG, Huang XY, Wang W, Powers JG. 2008. 'A description of the advanced research WRF version 3', Technical Note NCAR/TN-475+STR. NCAR: Boulder, CO

Schwartz, C. S., 2014: Reproducing the September 2013 record- breaking rainfall over the Colorado Front Range with high- resolution WRF forecasts. Wea. Forecasting, 29, 393–402, https://doi.org/10.1175/WAF-D-13-00136.1

Sitz, L. E., F. Sante, R. Farneti, R. Fuentes-Franco, E. Coppola, L. Mariotti, M. Reale, et al. 2017. "Description and Evaluation of the Earth System Regional Climate Model (RegCM–ES)." Journal of Advances in Modeling Earth Systems. doi:10.1002/2017MS000933

Song Y, Semazzi HMF, Xie L, Ogallo LJ, 2004: A coupled regional climate model for the Lake Victoria Basin of East Africa. Int. J. Climatol. 24: 57-75.

Sun X, Xie L, Semazzi F, Liu B, 2015: Effect of Lake Surface Temperature on the Spatial Distribution and Intensity of the Precipitation over the Lake Victoria Basin. Mon. Wea. Rev. 143: 1179-1192.

Sundqvist, H., Berge, E., and Kristjansson, J.: Condensation and cloud parameterization studies with a mesoscale numerical weather prediction model, Mon. Weather Rev., 117, 1641–1657,1989.

Talling, J. F. (1969) The incidence of vertical mixing, and some biological and chemical consequences, in tropical African lakes, Verh. Int. Ver. Limnol. 17, 998-1012 DOI: 10.1080/03680770.1968.11895946

Tiedtke, M., 1989, A comprehensive mass flux scheme for cumulus parametrization in large-scale models. Mon. Weather Rev., 117, 1779–1800

Tiedtke, M., 1993: Representation of Clouds in Large-Scale Models. Mon. Wea. Rev., 121, 3040–3061, https://doi.org/10.1175/1520-0493(1993)121<3040:ROCILS>2.0.CO;2

Tiedtke, M., . 1996: An extension of cloud-radiation parameterization in the ECMWF model: The representation of subgrid-scale variations of optical depth.Mon. Wea. Rev., 124, 745–750

Tompkins, A.: Ice supersaturation in the ECMWF integrated fore-cast system, Q. J. Roy. Meteor. Soc., 133, 53–63, 2007

Tripoli, G. J., and W. R. Cotton, 1980: A numerical investigation of several factors contributing to the observed variable intensity of deep convection over south Florida. J. Appl. Meteor., 19, 1037–1063.

Williams PD. 2009. A proposed modification to the Robert–Asselin time filter. Mon. Weather Rev. 137: 2538–2546

Weisman, M. L., C. Davis, W. Wang, K. W. Manning, and J. B. Klemp, 2008: Experiences with 0–36-h explicit convective forecasts with the WRF-ARW model. Wea. Forecasting, 23, 407–437, https://doi.org/10.1175/2007WAF2007005.1

Weusthoff, T., F. Ament, M. Arpagaus, and M. W. Rotach, 2010: Assessing the benefits of convection-permitting models by neigh- borhood vertification: Examples from MAP D-PHASE. Mon. Wea. Rev., 138, 3418–3433, https://doi.org/10.1175/2010MWR3380.1.

Zeng X, Zhao M, Dickinson RE (1998) Intercomparison ofbulk aerodynamic algorithms for the computation of seasurface fluxes using TOGA COARE and TAO data.J Clim 11: 2628–2644

Zhu, Y., and R. E. Newell, 1998: A proposed algorithm for moisture fluxes from atmospheric rivers. Mon. Wea. Rev., 126, 725–735, https://doi.org/10.1175/1520-0493(1998)126<0725:APAFMF>2.0.CO;2.